Vortex Dynamics in Transitional and Turbulent Boundary Layers

Peter S. Bernard*
University of Maryland, College Park, Maryland 20742

DOI: 10.2514/1.J051811

The dynamics of transitional and turbulent boundary layers is explored via a hybrid vortex filament/finite volume simulation scheme in which vortical structures are identified without the constraints imposed by the traditional assumption that they are synonymous with rotational regions. Vortex furrows consisting of elongated, streamwise-oriented, raised perturbations to the wall vorticity layer overlying low-speed streaks are found to be the principal structural element appearing during the Klebanoff-type transition. A number of dynamical properties of the furrows are considered, providing new insights into such questions as why hairpinlike rotational regions form that occur both singly and in pairs, why and how low-speed streaks form and why they persist, and why mushroomlike shapes and "pockets" are found in smoke visualizations of boundary layers. The physical picture of the boundary layer that emerges from the consideration of the dynamics of the vortex furrows provides some insights into why turbulence in the boundary layer is self-sustaining.

Nomenclature

R_e	=	Reynolds number
R_θ	=	momentum thickness Reynolds number
U, u	=	streamwise velocity and fluctuation
U_τ	=	friction velocity
V, v	=	wall-normal velocity and fluctuation
W, w	=	spanwise velocity and fluctuation
x	=	streamwise coordinate
y	=	wall-normal coordinate
z	=	spanwise coordinate
θ	=	momentum thickness

Superscript

$+$	=	wall variables

I. Introduction

THAT vortical structures play a major role in the dynamics of transitioning and turbulent boundary layers is well supported by evidence obtained from physical experiments and numerical simulations of turbulent wall-bounded flows. For example, rotational motion that likely has a vortical origin is visible directly in boundary layers using smoke or particles [1–5], and coherent, swirling motions appear in velocity data over three-dimensional (3-D) grids produced in numerical boundary-layer simulations [6]. Coherent regions of rotating velocity are also revealed to be present via isosurfaces of several scalar indicators of local swirl [7–9] when applied to grids of 3-D velocity data taken from numerical simulations [10–13] and physical experiments [14–18]. The presence of vortices is also indirectly indicated in such phenomena as low-speed streaks [19], ejections and sweeps [20], and "pockets" [21]. Identifying what the structures are and how they contribute to the dynamics of the boundary layer have long been primary aspects of boundary-layer research.

Presented as Paper 2012-750 at the 50th AIAA Aerospace Sciences Meeting, Nashville, Tennessee, 9–12 January 2012; received 5 January 2012; revision received 21 September 2012; accepted for publication 17 December 2012; published online 3 July 2013.

*Professor, Department of Mechanical Engineering. Associate Fellow AIAA.

For the most part, though not exclusively [22], it is customary to assume that coherent vortical structures in the boundary layer can be distinguished from the background flow by their primary property of having a distinct local swirling or rotating motion. Thus, the concept of "organized vortical structures" has become largely synonymous with "regions of rotational motion." From this point of view, the most commonly observed structures in transitioning and turbulent boundary layers have a form that may be described as that of a "hairpin" consisting of one or two streamwise-oriented "legs" connected downstream via an "arch" or "horseshoe" vortex. One-legged hairpins are often referred to as "canes." It has also been observed that hairpins often occur in groups called "packets" [23].

In a variety of contexts [6,24], it is known that the vorticity within hairpin-shaped regions of rotational motion in the boundary layer does not consistently have an orientation along the axis of the structures. To some extent, this is a natural consequence of the presence of considerable ambient spanwise vorticity generated at the wall surface that is ultimately the source of the vorticity within the hairpin structures themselves. When the local vorticity and the axis of the structures are misaligned, there is reason to suspect (by virtue of the extension of the vortex filaments to the surrounding flow) that the vorticity outside the structures may have some significant kinematic or dynamical connection to the vorticity within the structures. Consequently, by limiting the idea of structure to just the regions of rotational motion, the potential exists to overlook the true form taken by the local vorticity that acts as a coherent entity within the boundary layer. It should be noted that to some extent this concern has motivated recent efforts to include information about shear surfaces together with the rotational regions [25].

The practice of using isosurfaces of a scalar marker to denote the position and shape of coherent structures within the flowfield (and thus the need to decide on an appropriate contour level) adds an additional level of subjectivity to that inherent in the definition of vortical structures as regions of rotational motion. Although some ability to track structures defined this way through the flow has been achieved [26], in situations in which the rotational strength of a structure varies in space and/or time, as during its first appearance in the flow, it may be difficult to arrive at an objective understanding of the underlying phenomena. Closely related is the problem of discerning the true physical nature of multiple vortical objects that lie within close proximity to each other. Different parts of a structure are likely to have differing magnitudes of rotation besides the fact that there may be invisible, nonrotational vorticity connecting the separate objects.

The ambiguity inherent in the definition of structure according to its rotational field often means that multiple irreconcilable explanations for phenomena are possible. This is evident in

discussions concerning the connection between the velocity signatures of transition and the emergence of vortical structures [25,27–29]. For example, the shapes of rotational regions can be used to justify the existence of different kinds of vortical structures such as hairpin, ring, and U-shaped vortices [30,31] or other objects out of which different physical models of late transition may be developed. Similarly, the presence of low-speed streaks has been explained as due to the action of the lift-up mechanism [32] produced by streamwise vortices [33,34] as well as being the kinematic consequence of hairpin vortices organizing into packets [23,35]. The appearance of new hairpins in the flow has been accounted for as the end result of a secondary instability on low-speed streaks [34,36–38] as well as due to autogeneration processes [39,40] in which hairpins beget more hairpins. In a similar vein, previous explanations for such phenomena as the simultaneous appearance of both one- and two-legged hairpins [13,23,41] and retrograde vortices [42] do not preclude the possibility that such flow objects can be explained via a different set of physics based on a more comprehensive notion of what constitutes a vortical structure [43].

One means for visualizing the complete set of vorticity belonging to structures is to simulate the boundary layer using a vortex filament scheme. In this, the flowfield is represented via grid-free vortex tubes forming filaments that freely agglomerate to form large-scale structures that can be identified by inspection. For example, in jet flow simulations, vortex rings possessing various structural subtleties are readily depicted via filaments [44,45]. Likewise, in the case of shear layers [46,47], filament patterns in the form of roller/rib, chain-link fence, and oblique rollers with partial pairing are evident. Such forms match those seen in physical experiments. In previous work [48,49], boundary-layer flow was studied using a generalization of the filament scheme that accurately accommodates the production of vorticity at solid surfaces. Consistent with grid-based studies, hairpin-shaped regions of rotational motion were evident in transition, but they were found to represent the rotational signature of structures that may be best described as "vortex furrows": elongated, streamwise-oriented, raised folds in the surface vorticity layer. Some of the basic kinematical properties of the furrows were explored with just limited attention paid to their dynamics. The present study is focused on the dynamical aspects of furrows with a view toward revealing how their actions are consistent with a variety of flow phenomena that have long been observed in boundary layers. Among the issues to be considered are the relationship of the furrows to one- and two-legged hairpins, low-speed streaks, and mushroom-shaped and pocketlike smoke images as well as the mechanisms by which the turbulent field is self-sustaining.

The next two sections briefly review aspects of the numerical scheme and the computational problem that is solved. Following this, the basic makeup of the furrows is considered followed by a number of developments related to their dynamics. Lastly, some discussion of the breakdown of the furrows to turbulence at the end of transition is discussed, followed by conclusions.

II. Vortex Filament Scheme

The hybrid vortex filament scheme employed in simulating the boundary-layer flow is the same as has been previously described in detail [48]. It combines a finite volume solution to the full viscous vorticity equation on a thin prismatic mesh adjacent to the wall surface with a vortex filament calculation away from the boundaries. The vortex filaments are formed out of short, straight vortex tubes linked end to end with each tube defined by its endpoints and circulation. Vortex tubes on a common filament share the same circulation. At each time step, new vortices are created at the top layer of prisms from vorticity that has accumulated there from the wall-layer mesh computation. The circulation and orientation of the new tubes is set by requiring that the far-field velocity produced by the vorticity in the prisms and tubes should be identical. Some small local distortion in the velocity field is inevitable in this process.

The use of a grid next to solid walls is motivated by the need to accurately compute the steep vorticity gradients at the surface that control the viscous flux of new vorticity into the flow. A near-wall grid is generated outward from the surface triangularization and covers the region out to approximately $y^+ = 50$, where $y^+ \equiv yU_\tau/\nu$ and U_τ is the friction velocity. Because the Reynolds number is meant to be a real parameter in the simulations, the resolution of the boundary mesh aims toward that of a direct numerical simulation (DNS).

In the filament computation, the vortex tubes translate, stretch, and reorient according to the movement of their endpoints. Their circulation is taken to remain constant in time according to the approximate applicability of Kelvin's theorem, it being assumed that the Reynolds number is sufficiently high to make this a reasonable model in the flow removed from solid boundaries. Tubes that stretch beyond a limit are subdivided. Although viscous diffusion is not explicitly computed for the vortex filaments, vortex loop removal [50–52] is used to provide spatially and temporally intermittent dissipation at inertial range scales, with the important benefit of limiting the growth in the number of vortex tubes to manageable levels. The principle invoked here is that removing the loops (that naturally form to accommodate the boundedness of the energy as it flows to small dissipation scales) dissipates local energy that otherwise would be destined for removal at finer scales. Loop removal thus sidesteps the great expense of computing details of the motion including viscous vorticity diffusion at the tiniest scales.

The velocity field is recovered from a summation over the contributions of vortex prism sheets and vortex tubes by application of the Biot–Savart law. A potential flow derived from a distribution of surface sources is included as a means of enforcing the nonpenetration boundary condition. The computation of velocities is made affordable by the use of a parallel implementation of the fast multipole method [53,54] in which the cost scales linearly with the number of vortex tubes. Excellent parallel efficiency is achieved for up to approximately 22 processors.

III. Numerical Problem

The numerical simulation of the boundary layer performed in this study is in many respects similar to that considered previously [48]. In this, a spatially developing flow is computed on both sides of a wide flat plate of length 1.5, thickness 0.1, and span 2.5 in the streamwise, vertical, and spanwise (x, y, z) directions, respectively. Though the fluid arriving at the plate is free of disturbances, the transition from laminar to turbulent boundary layers on the top and bottom surfaces is triggered by slight perturbations intrinsic to the act of representing the flow via many discrete convecting vortex filaments. This may be contrasted with traditional grid-based simulations in which overt forcing of the boundary layer is commonly applied to encourage transition [13,55]. Depending on the size of the vortex tubes, the density of surface triangles, the Reynolds number, and the smoothness of the leading edge of the plate, the linear extent of the initial laminar regime can be significantly varied. In the absence of specific disturbances that might provoke other modes of transition, the Klebanoff-type transition is found to consistently occur in the plate flow wherein parallel low-speed streaks develop out of small perturbations in the upstream Blasius flow.

For the purposes of the present study, two main calculations are performed from which the structure of the boundary layer is analyzed. The first has Reynolds number $R_e = 1.2 \times 10^5$ at the rear edge, transitions relatively quickly, and reaches turbulent flow conditions by $x = 0.5$. The second calculation, which is designed to have a relatively longer transition region, has a slightly more streamlined front edge than the first case and a lower Reynolds number, $R_e = 7.5 \times 10^4$, so that turbulent flow conditions are delayed until approximately $x = 0.9$. The numbers of surface triangles used to represent the plate in the two calculations are, respectively, 74,274 and 98,080.

The relatively modest Reynolds numbers of the simulated boundary layers, implying an early onset to transition, reflect the combined influence of the blunt leading edges of the plates and the aforementioned sensitivity of the many interacting discrete vortex tubes to slight velocity perturbations associated with the use of the Biot–Savart law. Test calculations show that delaying transition by

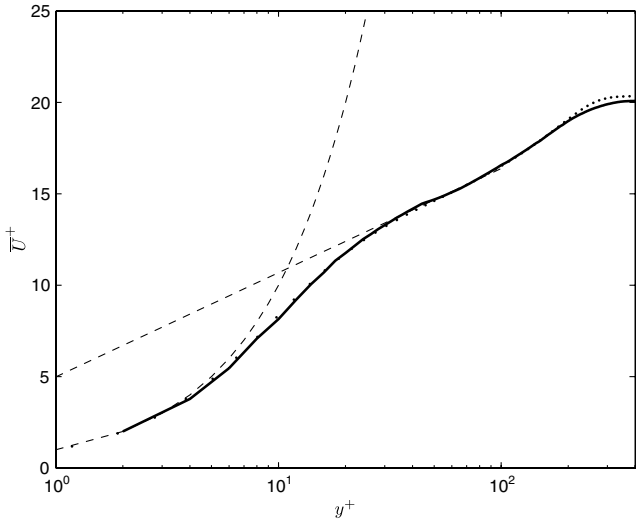

Fig. 1 Semilog plot of $\overline{U}^+$. —, vortex filament simulation; . . . , DNS [57] $R_\theta = 670$; — — —, $\overline{U}^+ = y^+$ and $\overline{U}^+ = 1/0.404\ \log(y^+) + 4.986$.

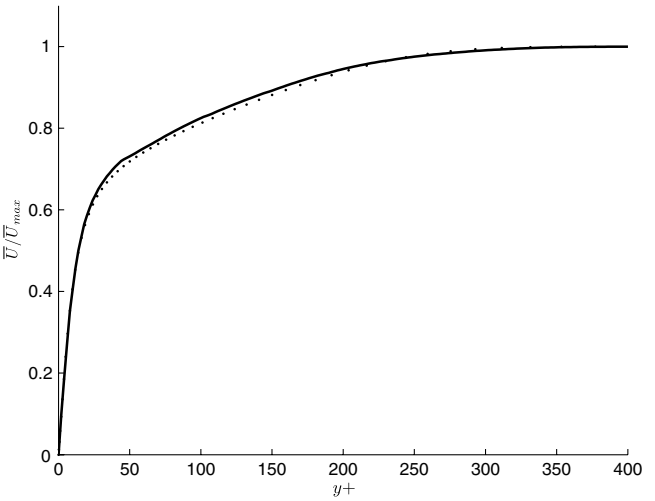

Fig. 2 $\overline{U}/\overline{U}_{\max}$. —, vortex filament simulation; . . . , $R_\theta = 670$ DNS [57].

increasing the resolution results in a substantially higher computational cost without materially affecting the properties of the vortical structures appearing in transition. For example, whereas the density of structures within the boundary layer increases with Reynolds number, the obvious physical nature of the structures remains the same.

The flow in the central part $|z| \leq 0.25$ of the plates constitutes a test section that has mean statistics independent of the spanwise position and is the exclusive focus of the following analyses. The test section in both cases is more than five boundary-layer-thicknesses wide and has dimensions in wall units of $(x^+, z^+) = (6177, 2059)$ for the higher-Reynolds-number case and (4890, 1630) for the lower-Reynolds-number case. Velocity statistics are computed from a time average of points distributed over the span of the central test section.

In both calculations, a prismatic mesh is erected from the surface triangles containing 11 layers with a layer of half-width adjacent to the boundary. Taking $y = 0$ at the plate surface, the mesh extends to $y = 0.012$. The number of surface triangles is more than 50% higher than in the previous study [48] yet still somewhat less than the degree of resolution normally associated with a high-quality DNS near the surface. For example, typical values within the turbulent domain of the thickness of the half-sheet on the wall surface for the present grids are, respectively, $\Delta y^+ = 2.60$ and 2.06, which implies that the spacings between triangles are approximately $\Delta z^+ = 45$ and 31. Finally, the maximum length of vortex tubes is taken to be 0.005 and 0.01 in the high- and low-Reynolds-number flows, respectively. These scale to approximately 20–30 in wall units.

The boundary-layer simulation begins from an impulsive start of the flow and runs in time until an equilibrium state is achieved. For example, in the simulation at $R_e = 7.5 \times 10^4$, a leveling off in the number of vortex tubes occurs at approximately time $t = 2$, with a slow relaxation to an equilibrium in the flow conditions well established by time $t = 2.85$. Once the equilibrium state is reached, the flow is computed for an additional 2.2 time units ($\Delta t^+ = 484$) for the higher-Reynolds-number case and 1 time unit ($\Delta t^+ = 213$) for the lower Reynolds number case. To limit the number of vortices in the calculation, a downstream boundary is defined such that all filaments passing this point are removed from the flow. The missing vorticity has some effect on the adjacent part of the flow just upstream. Consequently, attention is confined here to the flow upstream of $x = 1.2$. The number of vortex tubes when equilibrium conditions are reached in the two simulations is 26 million and 40 million, respectively.

Some evidence for the innate physicality of the computed boundary-layer flow is provided in Figs. 1 and 2, containing plots of the mean velocity field computed as an average over the data points within the fully turbulent zone $0.6 \leq x \leq 0.7$ for the simulation at $R_e = 1.2 \times 10^5$. In this region, the local value of the Reynolds number based on the momentum thickness R_θ varies between 602 and 623. The computed constants in the log law $\overline{U}^+ = 1/\kappa\ \log(y^+) + B$ are $\kappa = 0.404$ and $B = 4.986$ that agree well with a wide range of studies [56]. In Fig. 2, the comparison to the DNS data is made for the mean velocity scaled by the far-field velocity, and here, the agreement is quite excellent. Both of these results show that there is a relatively small and ultimately inconsequential distortion to the mean velocity in the neighborhood of $y^+ \approx 50$ deriving from the switch between prisms and tubes at this location.

IV. Vortex Furrows

The vortex filaments used in representing the flow outside the immediate wall vicinity can be made the basis for visualization of flow structures that are not readily depicted from traditional grid-based distributions of velocity and vorticity. For example, Fig. 3 provides a view of the computed vortex filaments in the boundary-layer simulation at $R_e = 7.5 \times 10^4$ from an overhead vantage point. The view includes the top surface of the plate from the leading edge at $x = 0$ to the position $x = 1.2$ at the right. The lateral boundaries are between $z = -0.25$ and 0.25. At the left, the incoming flow is laminar with spanwise-aligned vortex filaments. Transition begins upstream of $x = 0.4$ with a faint spanwise undulation to the vortices that gains in strength until elongated streamwise structures appear (the vortex furrows) in the region $0.4 \leq x \leq 1.0$. The average spanwise spacing of the furrows varies between approximately $\Delta z^+ = 150$ to 225 in viscous units, and they are approximately 1000 viscous units in length. Beyond $x = 1$, the flow becomes increasingly turbulent, and the organization of the filaments into furrows is less distinct.

Some idea of how the structure in Fig. 3 fits in with a more traditional view of the boundary layer is given in Fig. 4, in which the isosurfaces of the streamwise velocity fluctuation demarcating low- and high-speed fluid ($u = -0.3$ and $u = 0.15$) are displayed together with isosurfaces of rotational motion marked using $\lambda_2 = -100$. Here,

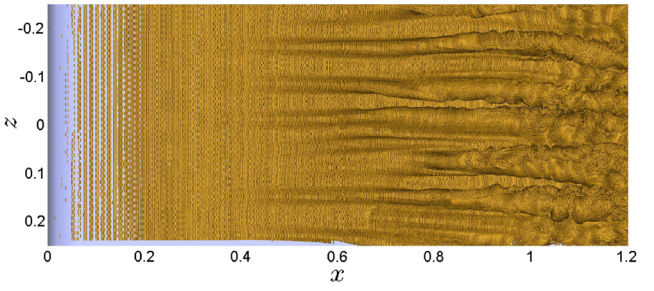

Fig. 3 Overhead view of vortex filaments in the boundary-layer simulation at $R_e = 7.5 \times 10^4$.

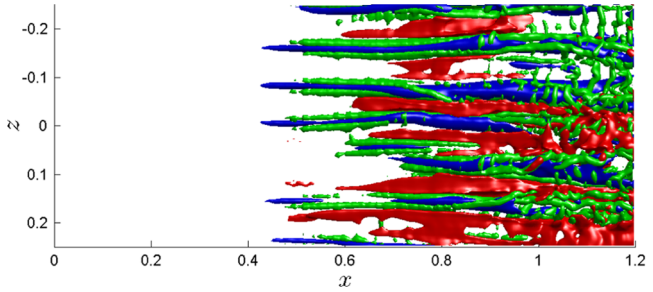

Fig. 4 During transition, isosurfaces marking low speed streaks are accompanied on one or both sides by isosurfaces of λ_2 indicating the presence of hairpinlike rotational regions. Between the hairpins isosurfaces of high-speed fluid reveal the presence of sweeping motions. The view is for the same time, domain and simulation as in Fig. 3.

λ_2 is the second eigenvalue of the matrix $S^2 + W^2$, where $S = (\nabla U + \nabla U^t)/2$ is the rate-of-strain tensor, $W = (\nabla U - \nabla U^t)/2$ is the rotation tensor, and $(\nabla U)_{ij} = \partial U_i/\partial x_j$. The rationale for using λ_2 to mark the rotational regions, as well as its effectiveness in doing so, has often been noted [7,9]. In the present case, λ_2 is found by first evaluating the velocity field on a mesh and then computing the necessary derivatives via finite difference formulas. Within the main part of the transition region before the onset of turbulence, Fig. 4 shows that the volumes of rotating fluid revealed by isosurfaces of λ_2 are in the form of either one- or two-legged hairpins. These straddle the low-speed streaks as seen in the Klebanoff-type transition and have a one-to-one correspondence with the furrows. The elongated regions of high-speed fluid are located adjacent to and outside the furrows. In a number of instances, the arch vortices are seen to connect the hairpin legs.

Among the hairpinlike objects in Fig. 4, some are in the form of nested arch vortices that have a resemblance to "hairpin packets." Considerable weight has been attached to the hairpin and hairpin packets in previous attempts at explaining the dynamics of transitional and turbulent boundary layers [23]. The evidence in Figs. 3 and 4 as well as prior studies [48,49] suggests that, whereas the hairpins are the rotational signature of the furrows, it is only the latter that are complete structures suitable for analysis of the boundary-layer physics. Consequently, the primary focus of the following discussion will center on elucidating the role of the furrows in a variety of phenomena associated with boundary layers, whereas the hairpins will be of subsidiary interest primarily because of their usefulness in identifying the location and rotational properties of the furrows.

Some idea of the interior of a typical furrow is given in Fig. 5, showing, from an end-on perspective, the collections of vortex tubes intersecting several planes along its length. The profile taken by this particular furrow at fixed x locations is seen to proceed from an archlike form at $x = 0.58$ to a mushroomlike shape by $x = 0.7$. The similarity of the latter with the mushroomlike images in smoke-filled boundary layers is unmistakable [3,58,59] and, moreover, appears to be closer to and more natural than the connection that is often assumed between the mushrooms seen in experiments and hairpin vortices [60]. By $x = 0.88$, there are the beginnings of a noticeable distortion away from the mushroomlike profile that signals the ending of transition. Streamwise-oriented vorticity is seen to concentrate within the lobes of the mushroomlike parts of the furrow with orientation in each lobe consistent with the wall-normal growth of the structure.

The connection between the furrows and the rotational volumes used in more conventional analyses of boundary-layer structure is given succinctly in Figs. 6 and 7. The first of these shows the upstream end of a furrow where it has an archlike form (indicated by the filaments on three cuts through the furrow) together with the isosurfaces of rotation. For the sake of clarity, the latter is rendered somewhat transparently. It is seen that the hairpin legs are associated with the sides of the arches for which the filaments are forward tilted and thus possessing streamwise vorticity that generates counter-rotating motion. This swirling flow is what gets represented graphically by the hairpin legs in the figure [48]. The filaments at the most downstream location in Fig. 6 are close to acquiring the mushroomlike shape that dominates the continuation of this furrow in the streamwise direction, as shown in Fig. 7. Here, consistent with Fig. 5, the vortex tubes with a streamwise orientation have become established within the lobes of the mushrooms as have the hairpin legs that represent the rotational motion produced by the streamwise vorticity. Thus, vorticity that only has a streamwise component due to tilting of filaments at the beginning of a furrow becomes fully oriented in the streamwise direction when the furrow acquires a mushroomlike form.

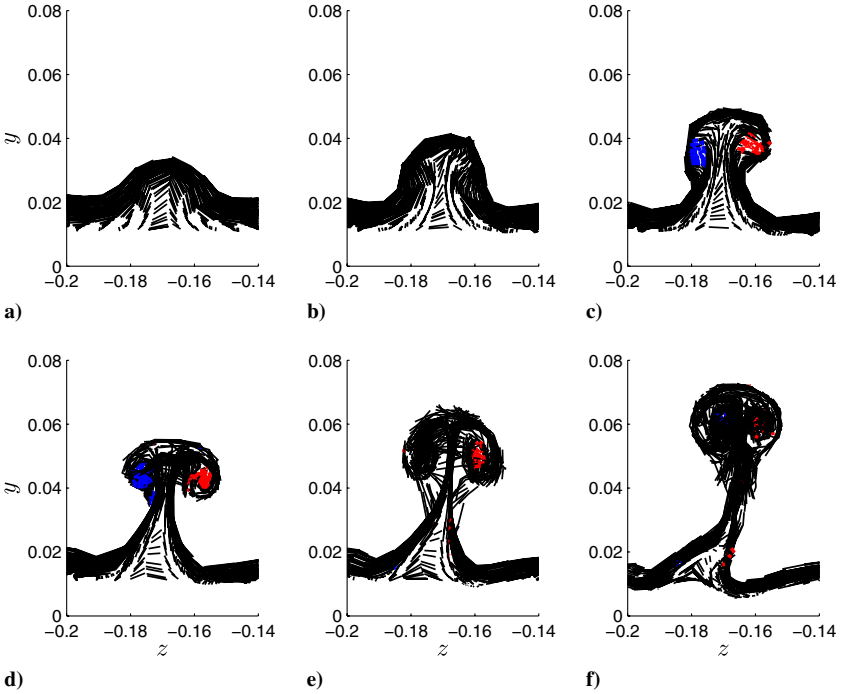

Fig. 5 End-on view of filaments on equally spaced spanwise cuts through a furrow at a fixed time: a) $x = 0.58$, b) $x = 0.64$, c) $x = 0.7$, d) $x = 0.76$, e) $x = 0.82$, and f) $x = 0.88$.

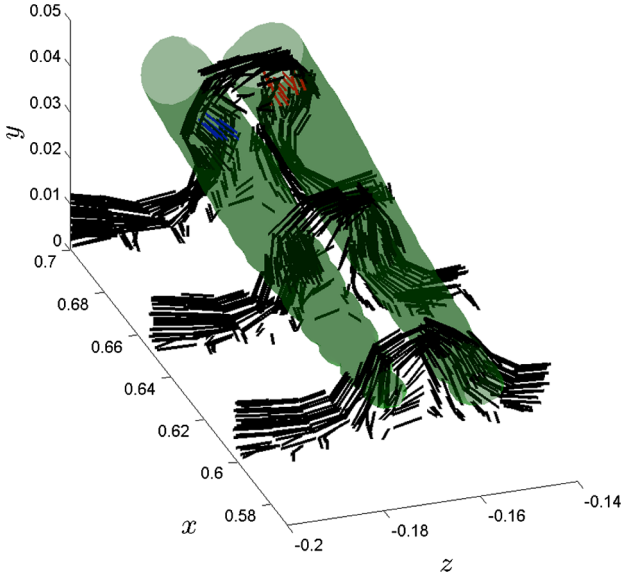

Fig. 6 Vortex filaments intersecting three spanwise planes near the upstream end of a furrow together with isosurfaces of λ_2 that represent the local rotational field.

Figures 6 and 7 help make clear the distinction between the vortex furrows that represent self-contained and complete vortical structures on the one hand and the hairpin vortices that represent just that part of the furrows having to do with their rotational motion. Nonrotational vorticity, both in the stem and across the top of the mushroom-shaped profile, plays a seemingly essential role in producing a structure that contains rotational motion in the form of hairpins. Subsequently, it will be seen that the form taken by the furrows, including the specific arrangement of vorticity within them, is determined by the dynamical process by which the streamwise-oriented vorticity is produced in the flowfield.

On many occasions, single-legged hairpins are observed in the filament simulations, as, for example, in Fig. 4 at $x = 0.6$, $z = 0.16$. Examination of the filament field underlying a typical example of this occurrence, as shown in Fig. 8, explains why just a single leg is visible and not two. Thus, in this case, the filaments comprising the furrow, as seen on spanwise planes at three locations, are tilted to one side with the mushroom lobe closest to the wall being the location of the single hairpin leg. Evidently, the roll-up process that forms the lobes and with it hairpins essentially atrophies on the side of the furrow tilted away from the wall, whereas the side closest to the ground plane strongly interacts with the wall vorticity leading to the development of a single streamwise column of rotational motion. As before, there

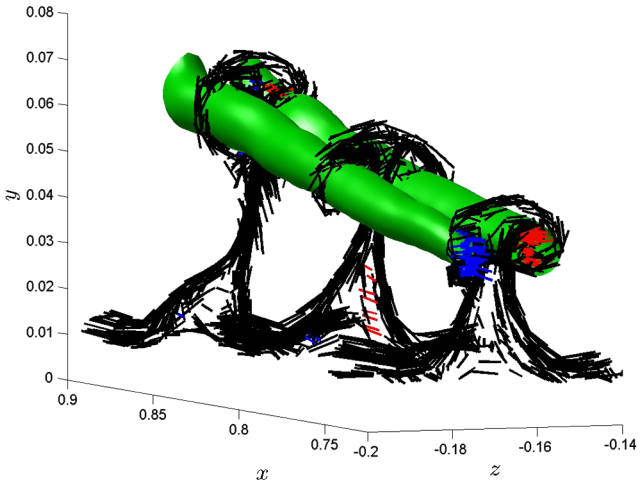

Fig. 7 Downstream continuation of the furrow in Fig. 6 showing isosurfaces of rotation filling out the lobes of filaments forming a mushroom shape.

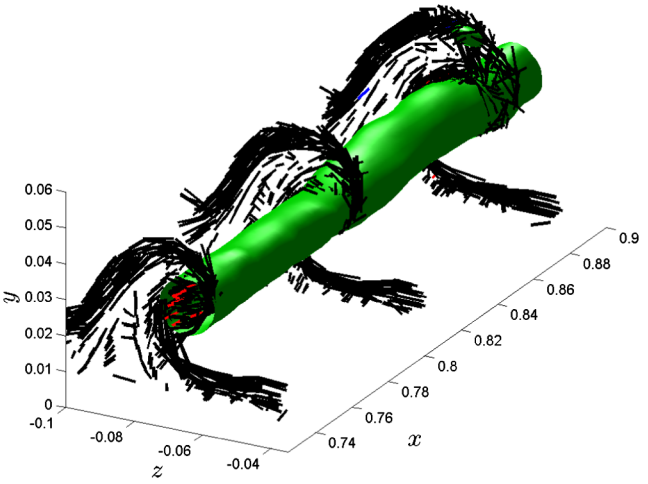

Fig. 8 Single hairpin leg representing the rotational signature of a tilted furrow.

is significant streamwise vorticity within the now single lobe of the mushroom. Despite having only one sense of rotation, low-speed fluid accumulates beneath the tilted furrow forming a streak and is ejected outward in very much the same way as happens for a symmetric mushroom having two hairpin legs.

The connection between the hairpin legs and furrows provided by Figs. 6–8 has the beneficial consequence of offering a relatively simple and unified explanation for why both one- and two-legged hairpins are observed in boundary layers. In fact, in all cases, they are the rotational signature of furrows, but sometimes the furrows acquire a tilt to one side or the other that promotes the growth of only a single leg. Why furrows tilt away from the symmetric state appears to be a result of an intrinsic instability, as will become evident next when considering the flow at the end of transition. It thus appears that noisy flow conditions (e.g., due to sound or other disturbances [61]) may promote a tendency for mushrooms to tilt, thus causing the more frequent observation of single-legged hairpins when rotational regions are mapped out.

V. Dynamics

Observation of the simulated flowfields reveals that the furrows occupy relatively stable positions within the flow, showing only minor shifts up- and downstream or laterally during extended time periods before moving off downstream to be potentially replaced by a new furrow. Despite the stability of the furrows as a whole, the filaments of which they are composed experience a variety of changes as they rapidly convect downstream within the furrows. This suggests that the physics of the flow associated with the furrows may be considered from both the point of view of the furrows in their entirety, including their formation and life cycle, as well as from the perspective of the processes affecting the development of the vorticity within them. How the two aspects of the furrows are related to each other can be understood after considering each of the dynamical properties separately.

A. Within the Furrows

The existence of a favored convection velocity that may be associated with coherent events within the boundary layer has often been measured and used in describing the evolution of structures [23]. In the present context, it is of interest to discern if there is a specific convection speed that may be associated with the movement of filaments along the plate and specifically within the furrows. One way to compute such a speed, if it exists, is by the translation along the plate of peaks in appropriate space-time velocity correlations. Specifically, the velocity at a given position, say $x = x_o$, $y = y_o$ at time t_o, can be correlated with upstream velocities at an earlier time via

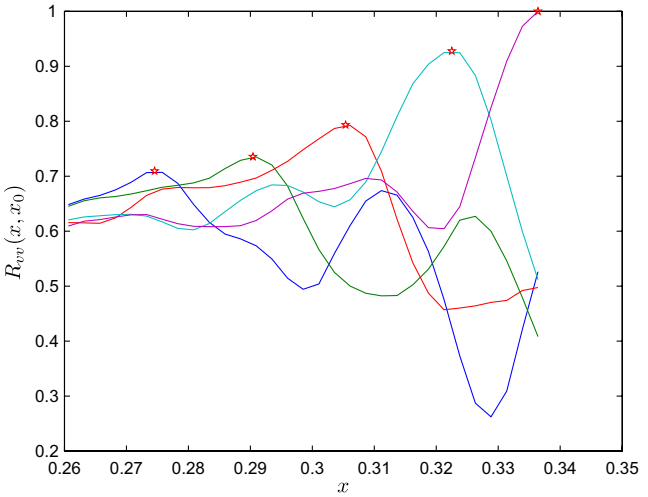

Fig. 9 Space-time velocity correlation in Eq. (1) evaluated for $x_o = 0.336$, $y_o = 0.026$. From right to left, the curves are for $t - t_o = 0$, -0.023, -0.043, -0.066, -0.085.

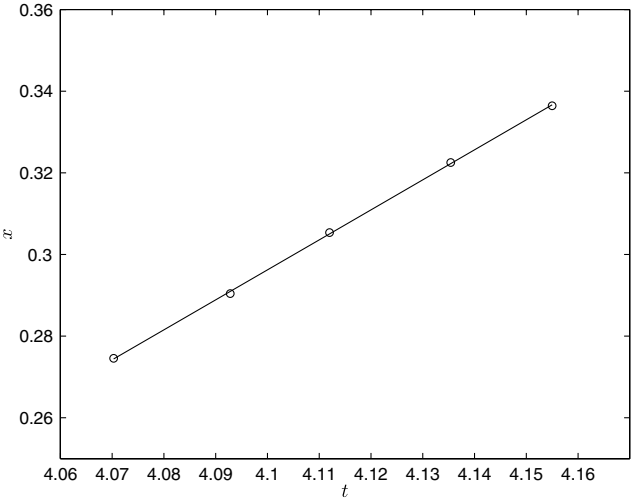

Fig. 10 Linear fit to correlation peaks in Fig. 9.

$$R_{vv}(x_o, y_o, t_o; x, y, t) = \frac{\sum_{i=1}^{N_z} v(x_o, y_o, z_i, t_o) v(x, y_o, z_i, t)}{\sqrt{\sum_{i=1}^{N_z} v(x_o, y_o, z_i, t_o)^2} \sqrt{\sum_{i=1}^{N_z} v(x, y_o, z_i, t)^2}} \quad (1)$$

where $v(x, y, z, t)$ is the wall-normal velocity in the boundary layer, $t \le t_o$, and the sums are over N_z equally spaced points covering the span of the test section. A typical result for R_{vv} in the late transition region at $x_o = 0.336$, $y_o = 0.026$ for the $R_e = 1.2 \times 10^5$ simulation is shown in Fig. 9. The presence of a favored correlation between upstream velocities at a given time and downstream velocities at earlier times is evident in the downstream shifting of maximum correlation with increasing time delay. Figure 10 shows the locations of the correlation peaks as a function of time. Evidently, to good accuracy, the translational speed of the peak is constant in time, and so there is little ambiguity in determining the implied convection velocity from a least-squares fit to the data. The convection speed in this case is computed to be 0.735, and values close to this may be computed for a wide range of nearby locations. If the data used in establishing the correlation is limited to the narrow region within a single furrow, then a similar result occurs as in Figs. 9 and 10 with the primary difference being a somewhat slower decay in the peak correlation amplitude and a lower convection velocity, typically around 0.67, that no doubt reflects the fact that low-speed streaks are centered within the furrows. The convection speeds computed here are in the same range as has been found in many prior studies.

By plotting the filaments in a furrow from the perspective of an observer moving with the previously determined convection speed, it becomes possible to see the general outlines of what the dynamics of the vorticity field looks like within the furrows. A view from above of the filaments in a furrow at four consecutive times is given in Fig. 11. The accumulation and concentration of significant streamwise vorticity along the length of the furrow is evident. To see how the vortex filament field develops in time within the furrow, an end-on view is provided in Fig. 12 of the vorticity within the small region outlined in Fig. 11 that is convecting downstream at speed 0.7. From

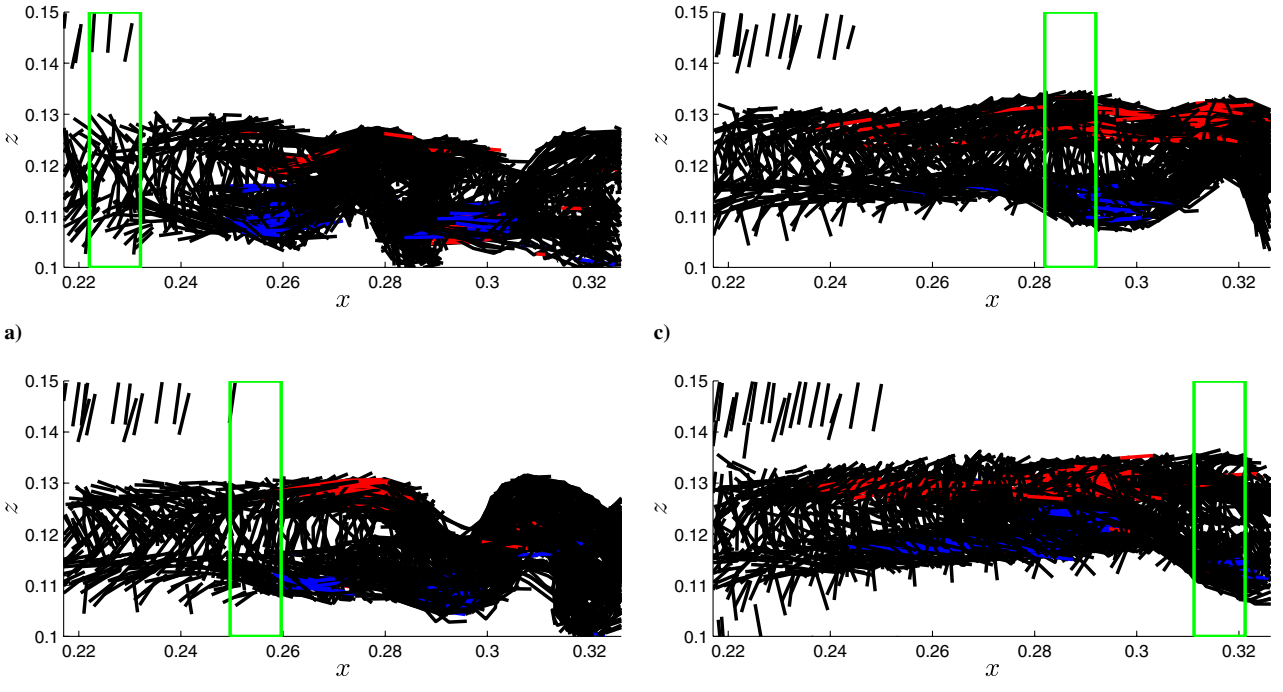

Fig. 11 Overhead view of vortex filaments in a furrow as it evolves in time: a) $t^+ = 0$, b) $t^+ = 10.9$ c) $t^+ = 23.9$, and d) $t^+ = 43.4$. Window moves at speed 0.7.

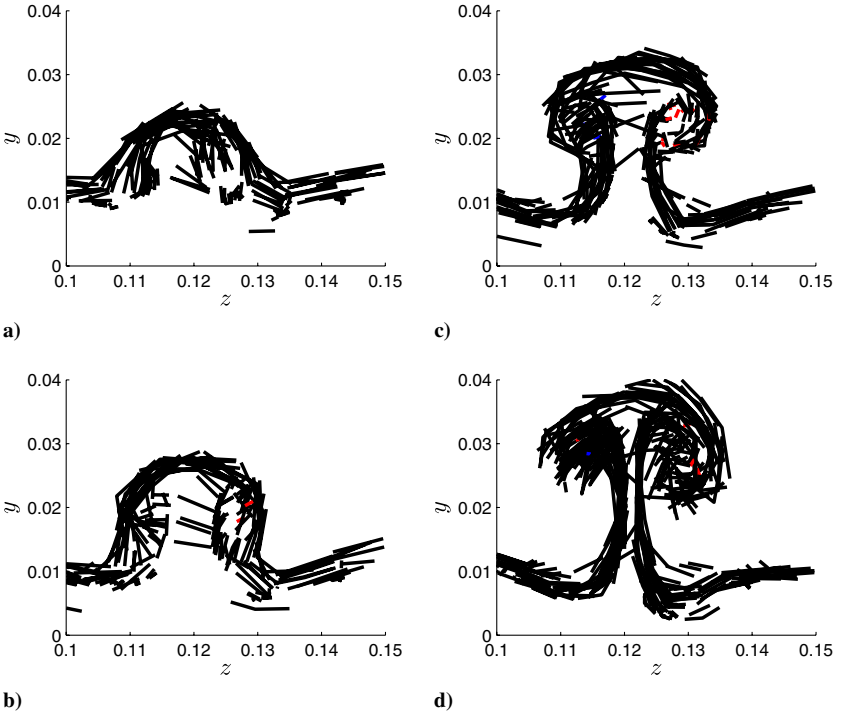

Fig. 12 Evolution in time of the filaments within the moving window in Fig. 11: a) $t^+ = 0$, b) $t^+ = 10.9$, c) $t^+ = 23.9$, and d) $t^+ = 43.4$.

this perspective, the vorticity is seen to pass through a sequence of states from arch- to mushroomlike forms, the same as what existed at a fixed time along the length of a furrow in Fig. 5. The distance over which the change in Fig. 12 takes place is approximately $\Delta x^+ = 575$.

It may be concluded that, during the lifetime of the furrow, which is substantially longer than the time interval captured in Figs. 11 and 12, the vorticity passes through it as if in an assembly line undergoing a continuous transformation from archlike to mushroomlike forms. While this process occurs, the furrow shifts slowly in position as does the location along the furrow where the filament profiles change from archlike to mushroomlike forms. In the example shown in Fig. 11, it is also the case that the furrow is subject to transitory disturbances that cause tilting of the mushroom structure. The sequence of images shows a distortion to the furrow that moves downstream with the result that the furrow returns to a symmetric form in the last view. This suggests that the furrows do not feed a steady stream of identically shaped mushroomlike vortical forms into the posttransitional flow downstream but rather a continuously changing array of structures that vary in angle and other qualities. This viewpoint will be seen to be supported by the analysis of the late transition considered in Sec. VI.

The sequence of images in Fig. 12, or equivalently, the images in Fig. 5 at a fixed time, gives some insights into how the mushroom shapes are created. For example, the wall-normal vorticity contained within the two sides of the archlike structures at the upstream end of the furrows is initially separated in the spanwise direction with a low-speed streak between them. As the archlike structures move downstream, the wall-normal vorticity at their sides is pushed toward the center by the counter-rotating motion associated with the furrow that includes the ejection of low-speed fluid outward from the middle. As the process continues, the relatively narrow stems of the mushroom-shaped vortices are formed as is also the general mushroom shape of the furrow itself. How the lobes acquire streamwise vorticity is a question that will now be considered.

B. Creation of Streamwise Vorticity

Although the mushroomlike profiles of the furrows appear to be a natural expression of the underlying counter-rotating motion associated with them, it is clearly the presence of streamwise vorticity in the lobes that drives the process forward by creating the counter-rotating motion in the first place. Thus, explaining the mechanism by which streamwise vorticity accumulates in the mushroom lobes so as to reinforce the counter-rotating motion first induced by forward-tilted vorticity within the archlike structures is a key step in understanding how the boundary layer works during transition and possibly also under turbulent flow conditions.

A view of the process by which the streamwise vorticity is generated can be had by following the time history of initially spanwise lines of tracer particles in the vicinity of the furrows. With a sufficiently fine-grained coverage, the tracers well account for the reorientation and stretching of material lines as they move in the flow. If it is assumed that the tracers are sufficiently far from the wall, so that the direct influence of viscosity can be neglected, then the material lines may be taken to also represent the convection of vortex filaments in the same locations. Note that the neglect of viscosity among the filaments within the numerical scheme is justified through the same set of assumptions. Analysis of the creation of streamwise orientation from initially spanwise-aligned material lines can go far toward explaining from whence the streamwise vorticity appears within the furrows.

Figure 13 shows the evolution of an initially spanwise material line at $x = 0.5$ that is purposefully chosen at an altitude and spanwise position that strongly interacts with a furrow, in this case, the furrow that is highlighted in Figs. 6 and 7. Tracer particles on the material element are initially equally separated so that the extent of localized stretching can be intuited from the subsequent spacing of elements. From the end-on perspective in Fig. 13, the material line is seen to initially rise upward as part of the ejecting low-speed fluid that is contained within the central part of the furrow. As the tracers rise, they curl up inside the lobe area of the flow due to the influence of the counter-rotating motion centered in the top part of the furrow. Substantial stretching of the material line across the top of the furrow is evident.

By the third image in Fig. 13, some streamwise orientation of the tracers begins to take hold at locations to either side of the rounded upward ejecting central part of the line. This is made clear in Figs. 14 and 15 showing the tracers from top and side views, respectively. The positions where the streamwise orientation becomes visible are where the high-speed sweeping fluid carried wallward due to the counter-rotating velocity field most closely encounters the ejecting low-speed fluid. The extent and degree of streamwise orientation grows in the subsequent views in Fig. 13, with the lobes of the mushroom shapes becoming the central location where the streamwise parts of the material line accumulate.

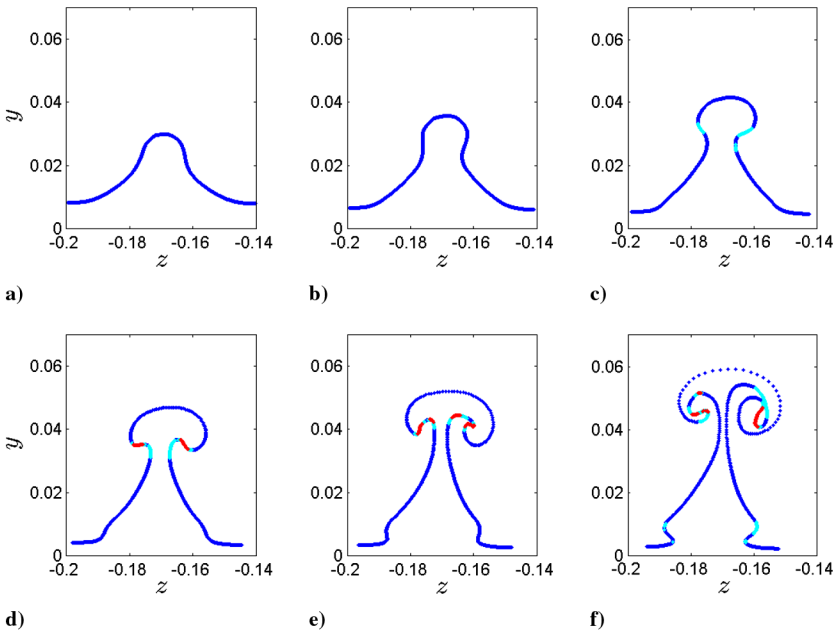

Fig. 13 End-on view of material line element: a)–f) correspond to equally spaced times over an interval of length $\Delta t = 0.192$ ($\Delta t^+ = 40.9$).

The top and side views of the tracers in Figs. 14 and 15, respectively, give a clearer view of the way in which the material line reorients into the streamwise direction. In particular, Fig. 15 shows how the tracers are initially pushed backward as they rise because they are immersed in ejecting low-speed fluid. At the same time, the rising tracers encounter faster-moving fluid and begin to be uniformly pushed forward, except at the points on the side where the high-speed fluid curves in toward the central plane of the furrow. Here, the large differential in the streamwise velocity between the ejecting fluid in the center of the furrow and the sweeping fluid coming inward from outside pulls the tracers into the streamwise direction. Initially, the turning of the line segment is caused primarily by the retarded fluid, as in the third and fourth images in Figs. 14 and 15, but subsequently, the figures show that the lengthening into the streamwise direction is also driven by faster-moving fluid. This may be a consequence of the continual rise in the streamwise line segments, as seen in the last images in Fig. 15, which would act

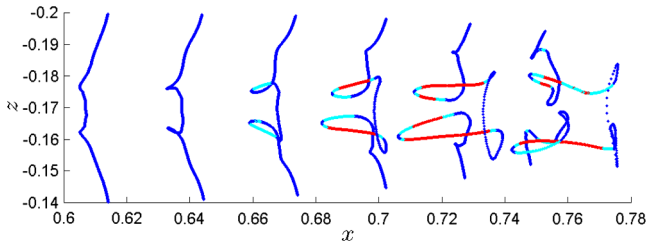

Fig. 14 Top view of material line element as it moves downstream at times corresponding to those in Fig. 13.

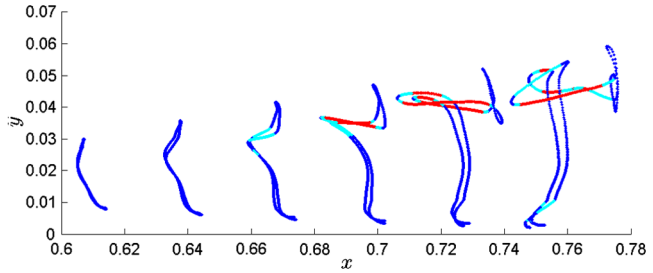

Fig. 15 Side view of material line element as it moves downstream at times corresponding to those in Fig. 13.

to increase the effect of the fast-moving fluid relative to that of the slow-moving fluid. The gathering of the rising streamwise tracers in the lobes fits in with the upward downstream tilt of the mushroom-shaped furrows, as seen in Fig. 7.

The physical model suggested by Figs. 13–15 of how initially spanwise material lines develop a streamwise component may account for the creation and augmentation of streamwise vorticity within the furrows. Thus, if the vorticity initially aligned in the negative z direction after having been created by shearing at the solid surface develops similarly to the material line element just discussed, then it is not hard to see that the plus and minus streamwise orientations of the vorticity arriving in the final positions in Fig. 14 are exactly what is required to generate the counter-rotating motion that drives the process forward. In essence, the counter-rotating motion generated by the archlike structures that first appear in transition causes the production of more streamwise vorticity that enhances the counter-rotating motion and thus causes the emergence of the mushroom-shaped structures with streamwise-oriented vorticity within their lobes. The phenomenon is thus self-reinforcing and a good candidate to be prevalent in the boundary-layer transition as well as under turbulent flow conditions.

In the case of tilted mushrooms associated with a single hairpin leg, as in Fig. 8, the streamwise vorticity appears to develop according to the same general mechanism as for a symmetric furrow. For example, Figs. 16 and 17 illustrate the motion of an initially spanwise material line as it interacts with the tilted furrow in Fig. 8. The end-on view in Fig. 16 shows that the rising tracers roll up into the one lobe of the mushroom. As before, the differential in speed between ejecting low-speed fluid and high-speed fluid sweeping around the mushroom lobe tilted toward the ground is most elevated at a point just below the lobe. Here, the tracers are redirected into the streamwise direction as they aggregate within the mushroom lobe, as seen in the sequence in Fig. 17.

C. Creation of Furrows

The boundary-layer calculations performed in this study begin by applying an impulsive start to the flowfield. As time progresses, an instability appears in the developing laminar flow that leads to the appearance of the furrows and eventually the fully developed turbulent field that forms downstream of the point where the furrows succumb to instability. Once established, the furrows appear to be relatively long lived in the sense that, for example, over the time $\Delta t^+ = 320$ of the simulation at $R_e = 7.5 \times 10^4$, a single furrow is observed to move off downstream and disappear with a new furrow

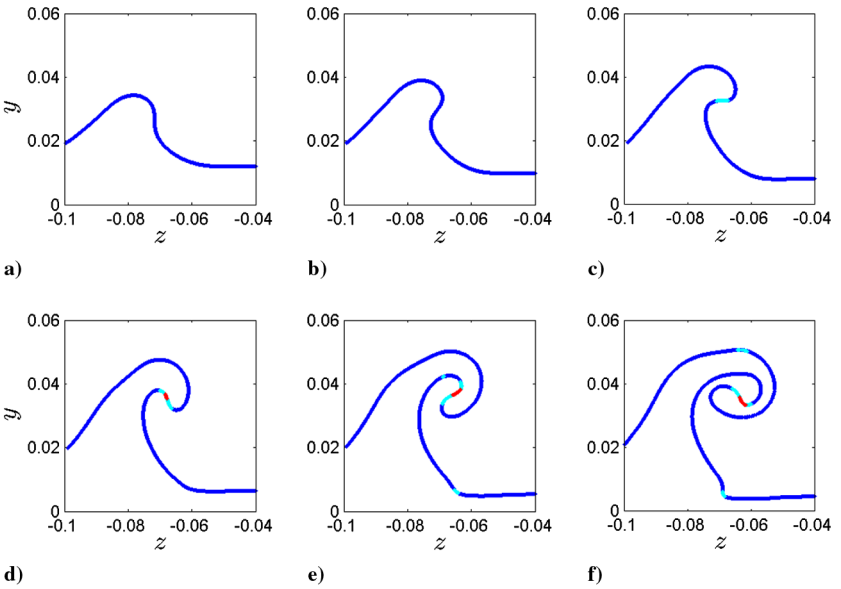

Fig. 16 End-on view of material line element associated with the single-lobed vortex in Fig. 8: a)–f) correspond to equally spaced times over an interval of length $\Delta t = 0.192$ ($\Delta t^+ = 40.9$).

taking its place. The specifics by which the changeover in the furrow occurs are shown in Fig. 18. First, the furrow that has reached the end of its life cycle is centered at $z = 0.075$. During the elapsed time between the two images in the figure, $\Delta t^+ = 38$, its upstream end moves from approximately $x = 0.6$ to 0.7. Second, indicated by the arrows, a new furrow grows from a relatively short disturbance extending over the interval $0.5 \leq x \leq 0.7$ in the first image to a much longer streamwise interval $0.5 \leq x \leq 0.85$ in the second image.

An examination of the filaments on the cross sections of the new furrow in Fig. 18a shows that they are arranged in the form of archlike vortices. In contrast, a short while later, the downstream part of the new furrow in Fig. 18b has developed mushroomlike vortices, whereas the upstream part remains archlike. It may be concluded that simple archlike perturbations in the background spanwise vorticity progress downstream acquiring mushroomlike forms and leaving

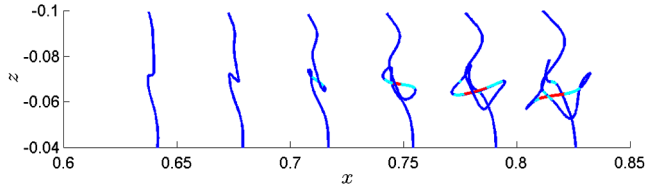

Fig. 17 Top view of material line element, moving downstream, at times corresponding to those in Fig. 16.

fully developed furrows in their wake. In other words, the same process discussed in the preceding section by which vortices traveling along the boundary layer within a furrow turn from archlike to mushroomlike forms is also responsible for the creation of new furrows.

Because low-speed streaks underlie the furrows, as was illustrated in Fig. 4, the process by which furrows develop in the flow also explains how and why low-speed streaks develop. In the first instance, the furrows have the capacity to concentrate low-speed fluid beneath their positions by virtue of the counter-rotating motion that is integral to their construction. As furrows develop in length and become elongated, so too will the spatial extent of the low-speed fluid that they foster. Thus, low-speed streaks of considerable streamwise extent are produced. By similar reasoning, the observed persistence of streaks for relatively long times in the flow corresponds to the similar persistence of the furrows.

An often-cited supposition [33,62] maintains that low-speed streaks are created by counter-rotating motion produced by the legs of hairpin vortices that are themselves created in the wake of downstream convecting arch or horseshoe vortices. An alternative model suggests that low-speed streaks are created as the kinematical consequence of the formation of hairpin packets [23]. In fact, the first of these ideas is essentially an indirect way of describing how the streamwise growth of furrows leads to the creation of streaks. Thus, because hairpin legs naturally appear as the rotational signature of furrows, the connection between hairpin legs and low-speed streaks

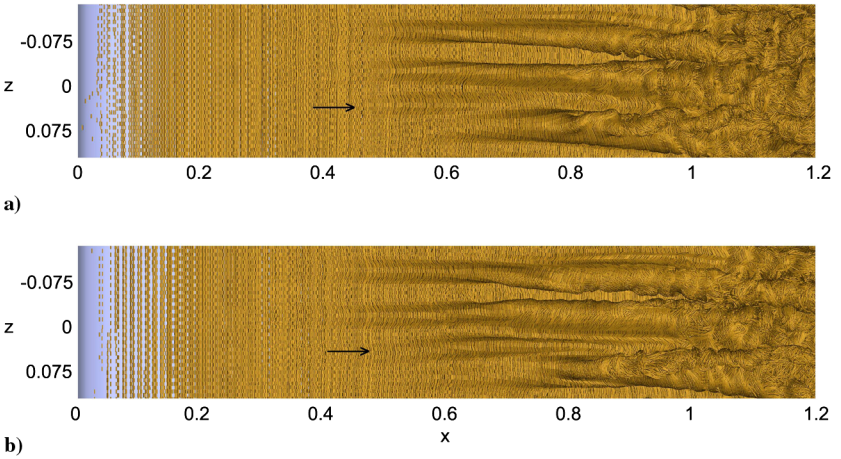

Fig. 18 As the furrow at $z = 0.075$ moves off downstream, a new furrow indicated by arrows develops nearby: a) $t^+ = 0$ and b) $t^+ = 38$.

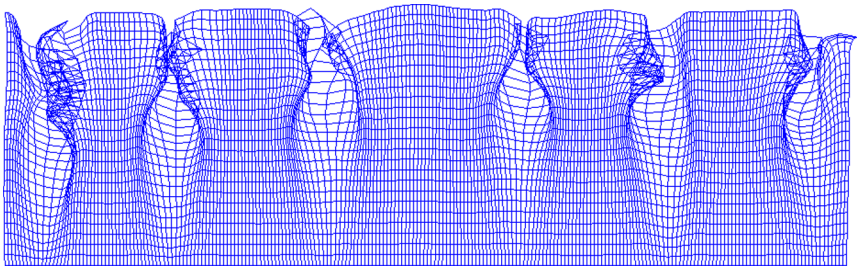

Fig. 19 Image of tracer particles modeling smoke in the boundary layer reveals the presence of pockets corresponding to vortex furrows. Direction of flow is upward.

may be viewed as a byproduct of the prima facie connection that furrows have with the streaks.

D. Pockets

Smoked-marked boundary layers, when viewed from above, have been observed [21] to contain "pockets" consisting of distinctively shaped regions that are largely devoid of smoke. Such structures are also visible in numerical boundary layers [63] by using a sufficiently large number of tracer particles to model the appearance of smoke. Explanations that have been given to account for the existence of pockets tend to require the action of a variety of special vortical objects whose existence has yet to be firmly established. Thus, it is of interest to discover if pockets are present in the filament simulations of the boundary layer and, if so, find out what connection they might have with the vortex furrows.

To model the presence of smoke in the computed boundary layer at $R_e = 1.2 \times 10^5$ equally spaced tracers on a line spanning the test section at $x = 0.2$ and $y^+ = 50$ were released at uniform time intervals. At this location, which is within the transition region, a series of furrows exist very much the way they do in Fig. 3 at the lower Reynolds number. Releasing particles into the flow at this location is a convenient means of seeing if a connection exists between furrows and pockets because the former is the only kind of vortical structure in the flow in this region. In fact, the computed motion of the tracers, as shown in Fig. 19 over the time interval $\Delta t^+ = 30.4$, shows that structures with the appearance of pockets form for each of the furrows in the field of view. In this, lines oriented mainly in the flow direction represent streamlines, whereas spanwise lines connect groups of particles that are placed into the flow at the same time step. Characteristic of pockets, the structures contain regions largely scoured of tracers and in this and other details are reminiscent of the tracer-marked objects seen in a previous computation of a spatially developing transitioning boundary layer [64]. Where furrowlike structures appear in the fully turbulent region, a similar connection to pocketlike images of tracers can be seen to occur.

A 3-D view of how the counter-rotating motion associated with a furrow causes the appearance of a pocket is given in Fig. 20. In this, the tracers inside the furrow decelerate while ejecting outward through the center, whereas tracers to the side are accelerated downward toward the wall. The stretching across the top of the furrow that was evident in Fig. 13f is responsible for clearing away tracers toward the sides where they roll up in the lobes to create the distinctive edging of the pockets. The characteristic shape of the pockets can be attributed to the fact that the sideways spreading of the smoke precedes the cumulative effect of the roll up in gathering particles into the region of the lobes. The demarcated boundary of the pockets tapers downstream because the longer the particles are influenced by the velocity field produced by the furrow the more they have circulated through the lobes. For some of the pockets, such as the second one from the right in Fig. 19, roll up of the tracers occurs on just one side suggesting that the underlying furrow is tilted and has just a single hairpin leg.

E. Hairpins

Hairpin vortices as revealed by the isosurfaces of rotation often contain archlike regions that either connect the two legs of a symmetric hairpin or form the top part of a one-legged cane vortex. Normally, the rotational motion in the archlike part of the hairpin is taken to be the direct consequence of vorticity aligned along the axis of the structure. Such an explanation is compatible with the tendency of hairpins to project outward above the intense spanwise vorticity lying adjacent to solid surfaces. In the same vein, the hairpin packet model interprets the appearance of multiple archlike regions of rotation as the signature of multiple hairpins that have developed together to form a packet. Because hairpin legs were shown previously to represent the rotational signature of furrows, it is of interest to see in what way the archlike regions of rotation in hairpins might also fit in with the underlying presence of furrows.

It may be noticed at several positions in Fig. 4 [e.g., $(x, z) = (0.9, 0.1), (0.9, -0.15), (1, -0.08)$] that arched vortices positioned over low-speed streaks seemingly connect the adjacent hairpin legs. Thus, the present simulations share this kind of rotational structure with many boundary-layer simulations and experiments [13,33,61]. A close-up view of the isosurfaces of rotation for a typical event of this kind taken from the $R_e = 1.2 \times 10^5$

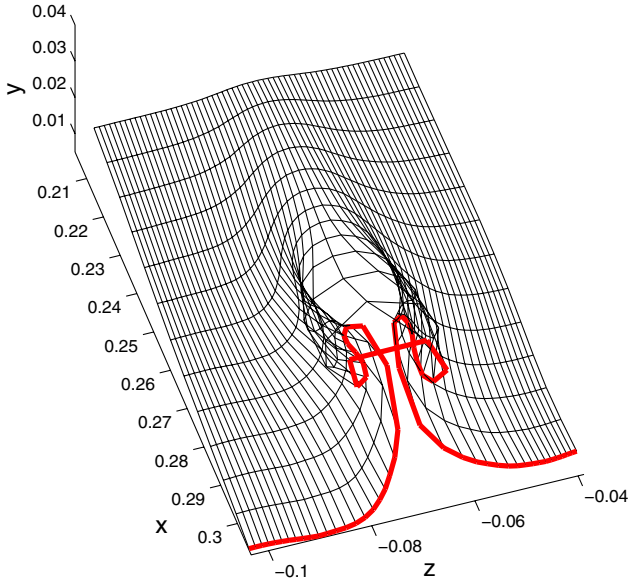

Fig. 20 Effect of a furrow on particles simulating smoke in the boundary layer.

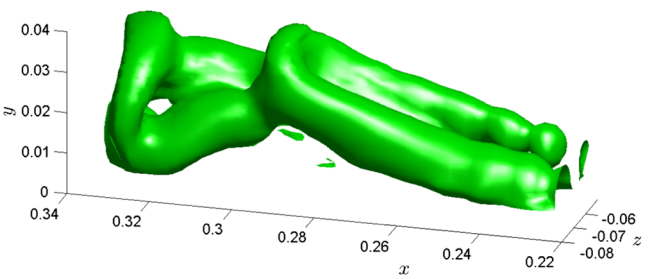

Fig. 21 Isosurfaces of $\lambda_2 = -60$ suggesting the presence of two hairpin vortices in the $R_e = 1.2 \times 10^5$ simulation.

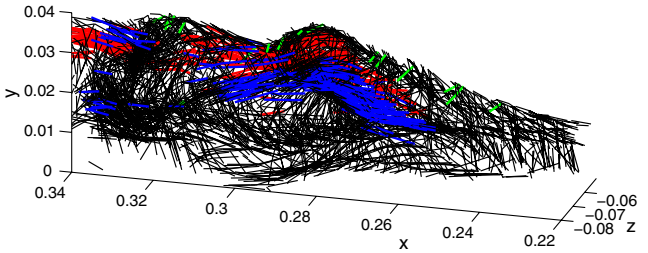

Fig. 22 Vortex filaments underlying the event in Fig. 21 seen from the identical angle.

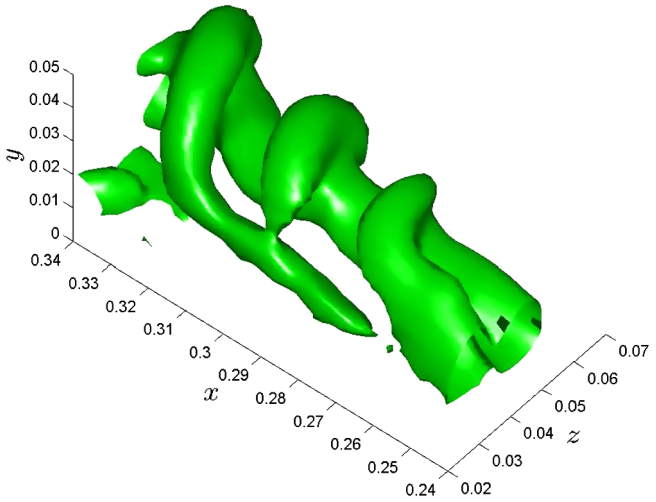

Fig. 23 Isosurfaces of $\lambda_2 = -30$ suggesting the presence of three archlike vortices in the $R_e = 1.2 \times 10^5$ simulation.

simulation is given in Fig. 21. A well-formed hairpin is seen to be present in the foreground with a second one attached to it and situated just downstream. Traditionally, this arrangement tends to be interpreted as meaning that two hairpin vortices are present that likely originated out of a common disturbance to the upstream boundary layer. The vortex filaments underlying this pair of hairpinlike regions of rotation are shown in Fig. 22 from the same perspective as in Fig. 21. The object that is revealed from the filaments is seen to be a somewhat perturbed furrow in which some spanwise vorticity has accumulated as bulges at those positions where the apparent archlike vortices in Fig. 21 are visible. Perhaps the most notable aspect of the figures is the subtlety with which the positioning of filaments leads to quite distinctive regions of rotation.

The concentrated formations of streamwise vorticity in Fig. 22 are indicative of a mushroomlike profile to the furrow that persists through the locations where the arch vortices occur. The regions where the spanwise vorticity concentrates on the top of the furrow presumably arise from shear-layer roll up due to interaction with the high-speed outer flow. In this case, the arched vortices appearing in Fig. 21 have a very different interpretation than that of being the top part of well-defined hairpin vortices.

An example of another commonly observed rotational structure in the filament simulation is depicted in Fig. 23. Here, three arch- or canelike rotational regions are connected with a single hairpin leg. Such structures are suggestive of the organization that is often described as being associated with a hairpin packet, but the underlying filaments, shown on several cuts in Fig. 24, reveal that the causative flow structure is a tilted furrow. In fact, images similar to those in Fig. 24 can be seen at any cross section of the structure in Fig. 23, with the main variation being that the size of the tilted mushroom depends on whether the cut is within or outside one of the bulges. For example, the structures in Figs. 24d and 24e appear larger than the others because they are within the arch segments, and the others are not. As in the case of Fig. 21, the three spanwise-oriented archlike regions in Fig. 23 result from roll up of the highly stretched spanwise vorticity at the top of the furrow and cannot be regarded as independent arch vortices.

The specific examples of archlike structures considered in Figs. 21 and 23 are representative of many other similar events seen in the filament simulations. Evidently, whether or not the furrows are symmetric or tilted, they can project substantial spanwise vorticity into the fast-moving outer flow where shear-layer instabilities promote the roll up of the vorticity into a form for which the rotational signature is that of single or nested hairpinlike structures. Once such processes start, the potential increases for the furrows to devolve into complex forms, and the flow becomes turbulent. Some basic aspects of this process as it affects the breakdown of furrows into turbulence is now considered.

VI. Breakdown to Turbulence

The shear instability out of which the rotational regions in Figs. 21 and 23 appear may be viewed as an initial stage in a sequence of dynamical events by which the furrows breakdown toward a turbulent state. Ever more complex distortions of the vorticity in the

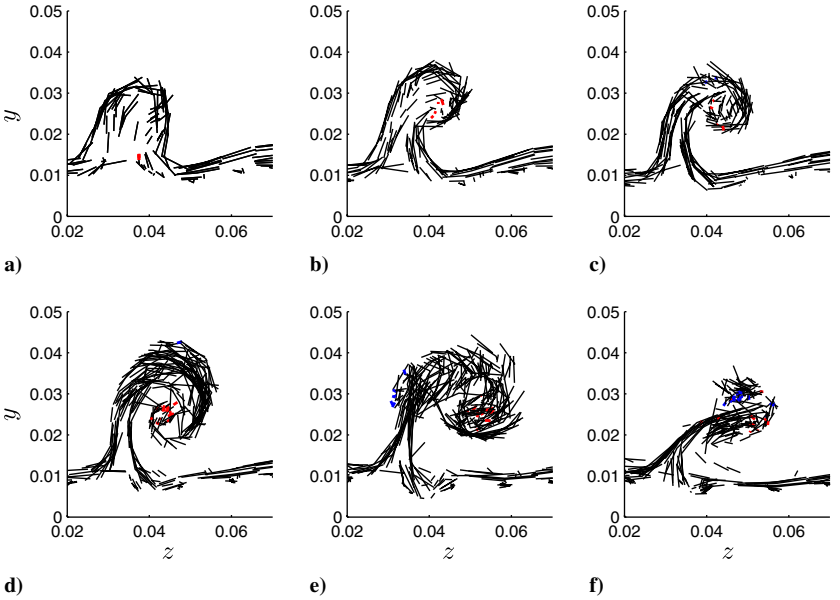

Fig. 24 End-on view of filaments within the structure in Fig. 23: a) $x = 0.24$, b) $x = 0.26$, c) $x = 0.28$, d) $x = 0.3$, e) $x = 0.32$, and f) $x = 0.34$.

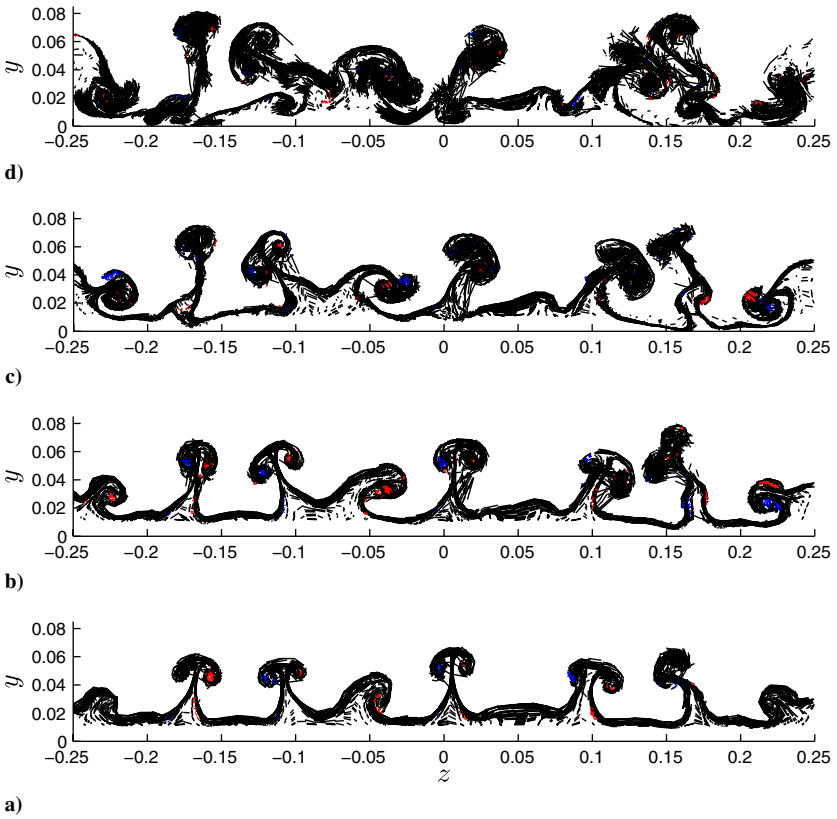

Fig. 25 Filaments at a fixed time showing progression to turbulent flow at the end of transition: a) $x = 0.8$, b) $x = 0.85$, c) $x = 0.90$, and d) $x = 0.95$.

furrows beyond the point illustrated in the preceding section occurs as the vorticity in the furrow moves into the turbulent region. Some indication of this is evident in Fig. 3, in which the furrows spread laterally and interact with neighboring furrows creating structures of greater complexity than those upstream.

A different perspective on the processes at work at the end of transition and into the turbulent region is provided by Fig. 25, in which the profiles of the filaments at several streamwise positions in the $R_e = 7.5 \times 10^4$ simulation are shown at a fixed time. The organization into mushrooms that is largely intact in the most upstream location at $x = 0.8$ is virtually nonexistent by $x = 0.95$. Individual mushrooms are seen to follow different paths to a more chaotic state over the spatial extent in the figure. Thus, those centered at $z = -0.23$, -0.04, and 0.225 tilt over until they are almost upside down and are intensely interacting with the surface vorticity. Others, at $z = -0.175$ and 0.01, appear to twist sideways, whereas those at $z = 0.1$ and 0.16 tilt toward each other, initiating a strong mutual interaction. It may be concluded that the furrows are either intrinsically unstable or are sensitive to the disruptive influence of nearby perturbations that promote the likelihood of breakdown. As mentioned in the preceding sections, the predilection for tilting when disturbed provides an explanation for why single-legged hairpins are more prevalent than two-legged hairpins in noisy flow conditions.

An interesting side light to the tendency for furrows to tilt is the effect that this may have on their rotational signature. For example, Fig. 26 illustrates a case in which extreme tilting of a furrow toward the ground plane is accompanied by twisting of the hairpin legs that have developed within the mushroom lobes. Without knowledge of the underlying filament field, very different explanations for the appearance of the crossed hairpin legs can be imagined. In fact, such structures appearing in rotational fields play an important role in recent analyses of the growth of secondary instabilities on low-speed streaks leading to breakdown [34,38]. Clearly the evidence in Fig. 26 warrants reinterpretation of streak breakdown from the point of view of the downstream development of instabilities in the furrows.

In a number of different ways, the preceding discussion has made clear that the literal interpretation of structure via isosurfaces of rotation is likely to oversimplify the nature of the true vortical forms giving rise to rotation in the first place. The capacity for distortion can only increase as the flow becomes fully chaotic in the turbulent zone, and the shapes taken on by regions of strong rotation, such as those depicted at the downstream side of Fig. 4, give little clue as to what may be inferred about the underlying vorticity field. Note, as well, that in this case the vorticity filament field itself, such as that shown in Fig. 3, is not readily interpreted in terms of simple vortical objects.

Despite these obstacles, some general observations can be made about vortical structures in the turbulent region. In particular, Fig. 3 suggests that the vorticity enters the turbulent zone in groups of somewhat affiliated structures that form along the furrows during

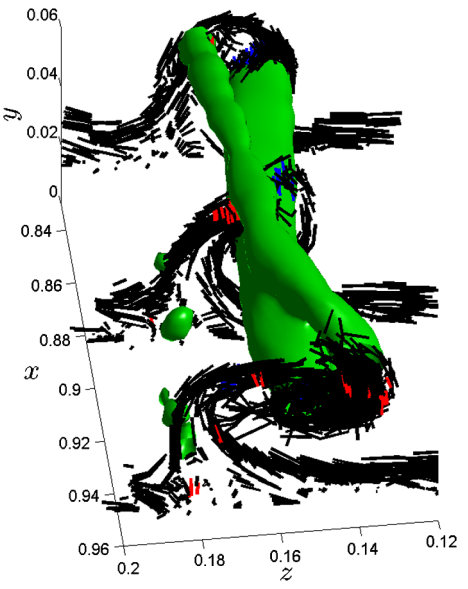

Fig. 26 Twisting of a furrow near the end of transition.

their breakdown, rather than as a continuous stream of vorticity. In other words, segments of the posttransitional furrows detach in some sense from the more stable upstream parts and become self-contained structures in the immediate wake of the transition region. The forms taken by these vortices are far more varied than the simple arches and mushrooms that dominate transition because the result of interacting with neighboring vortices and the wall leads to an endless variety of structural forms. Differences in structures from one place to another depend on how the vorticity in the furrows tilts, twists, and bends and whether it detaches from the wall layer or interacts with the ground plane.

Vortical structures that share a common origin in a particular furrow can be imagined to maintain some degree of self-coherency within the boundary layer as they convect for some distance downstream. A sense of this organization is visible in Figs. 3 and 4 as a continuing delineation between vortices originating in neighboring furrows that only slowly lessens with downstream distance. Eventually, as depicted in a prior simulation [48], this kind of coherency is no longer obvious to the naked eye. The downstream maintenance of a relationship between vortices that have derived from a particular furrow may be equivalent to the internal organization attributed to hairpin packets as they grow due to the multiplication of hairpin vortices [12]. The difference between the present result and packets is that the underlying structure formed out of furrows is not readily describable in the simple terms of a collection of nested hairpin vortices.

VII. Conclusions

This study has considered the structural aspects of boundary-layer flow determined from simulations based on a hybrid vortex filament/finite volume scheme. The natural tendency of vortex filaments to agglomerate to form coherent structures allowed for the determination of structure unrestricted by the imposition of its traditional definition in terms of regions of rotational motion. Vortex furrows were found to be the dominant structural entity in the transitional boundary layer subject to Klebanoff-type instability. Hairpin vortices that are widely touted as representing a dominant aspect of turbulent boundary layers are found to represent the rotational motion associated with furrows and have no standing as structures in their own right.

The view of the boundary-layer dynamics provided by the furrows offers a unified and relatively simple explanation for a range of disparate phenomena that have been difficult to account for in a systematic way using the traditional view of structure as rotational regions. Thus, one- and two-legged hairpins represent the rotational signature of tilted and symmetric furrows, respectively. The intrinsic instability of the symmetric mushroomlike form means that noisy flow conditions are likely to favor one-legged over two-legged hairpins. Low-speed streaks appear simultaneously with the furrows whose innate counter-rotating motion concentrates low-speed fluid beneath them. The length of the streaks coincides with the length of the furrows, and the persistence of the low-speed streaks for long times is consistent with the persistence of the furrows. Structures marked by smoke with the appearance of pockets and mushrooms are seen to reflect the direct influence that vortex furrows have upon smoke within the boundary layer. The robust mechanism within the furrows that promotes the generation of streamwise vorticity can be seen as providing a basis for understanding how and why the turbulence is self-sustaining. This process both creates furrows in the first place and maintains them over long time periods as the vorticity passes through them from archlike to mushroomlike forms.

The innate sensitivity of the furrows to disturbances leads to their breakdown and the commencement of the turbulent regime. Among the factors affecting the furrows is an apparent shear-layer-type instability on the top surface exposed to the freestream velocity that causes roll up of the spanwise vorticity and the appearance of archlike vortices in the rotational field. Other influences on the furrows lead to their tilting, twisting, and interactions with neighboring structures and the wall vorticity. The complex mushroomlike forms produced by the furrows dispel into the posttransitional region as discrete collections of filaments. The lingering coherence of structures arriving into the turbulent field from particular furrows may be reflected in some of the organization taken to be that of hairpin packets. In general, the filament configurations underlying packet-like regions do not appear to be in the form of nested hairpin vortices. Finally, there is evidence to suggest that the kinds of processes centered on furrows that have been presented here are also common to the fully turbulent field when local conditions are favorable.

The formalism for investigating the physics of the boundary layer provided by the vortex furrows has the potential to advance understanding in a number of directions beyond those considered here. These include elucidating details of the instabilities during transition, explaining the structural makeup of turbulent spots, and providing clearer insights into the nature of the complex filament field in the turbulent region. Each of these areas will be considered in future work. It is also the case that a number of the descriptions of the furrows provided here may be amenable to verification from grid-based direct numerical simulation computations, and it is hoped that such efforts will be forthcoming in the future.

Acknowledgments

This research was supported in part by the National Science Foundation through Extreme Science and Engineering Discovery Environment resources provided by the Pittsburgh Supercomputing Center.

References

[1] Offen, G. R., and Kline, S. J., "Combined Dye-Streak and Hydrogen-Bubble Visual Observations of a Turbulent Boundary Layer," *Journal of Fluid Mechanics*, Vol. 62, No. 2, 1974, pp. 223–239. doi:10.1017/S0022112074000656

[2] Praturi, A. K., and Brodkey, R. S., "A Stereoscopic Visual Study of Coherent Structures in Turbulent Shear Flow," *Journal of Fluid Mechanics*, Vol. 89, No. 2, 1978, pp. 251–272. doi:10.1017/S0022112078002608

[3] Head, M. R., and Bandyopadhyay, P., "New Aspects of Turbulent Boundary-Layer Structure," *Journal of Fluid Mechanics*, Vol. 107, 1981, pp. 297–338. doi:10.1017/S0022112081001791

[4] Smith, C. R., Walker, J. D. A., Haidari, A. H., and Sobrun, U., "On the Dynamics of Near-Wall Turbulence," *Philosophical Transactions of the Royal Society London A*, Vol. 336, No. 1641, 1991, pp. 131–175. doi:10.1098/rsta.1991.0070

[5] Kaftori, D., Hetsroni, G., and Banerjee, S., "Funnel-Shaped Vortical Structures in Wall Turbulence," *Physics of Fluids*, Vol. 6, No. 9, 1994, pp. 3035–3050. doi:10.1063/1.868129

[6] Bernard, P. S., Thomas, J. M., and Handler, R. A., "Vortex Dynamics and the Production of Reynolds Stress," *Journal of Fluid Mechanics*, Vol. 253, 1993, pp. 385–419. doi:10.1017/S0022112093001843

[7] Jeong, J., and Hussain, F., "On the Identification of a Vortex," *Journal of Fluid Mechanics*, Vol. 285, 1995, pp. 69–94. doi:10.1017/S0022112095000462

[8] Haller, G., "An Objective Definition of a Vortex," *Journal of Fluid Mechanics*, Vol. 525, 2005, pp. 1–26. doi:10.1017/S0022112004002526

[9] Chakraborty, P., Balachandar, S., and Adrian, R. J., "On the Relationships Between Local Vortex Identification Schemes," *Journal of Fluid Mechanics*, Vol. 535, 2005, pp. 189–214. doi:10.1017/S0022112005004726

[10] Robinson, S. K., "Coherent Motions in the Turbulent Boundary Layer," *Annual Review of Fluid Mechanics*, Vol. 23, 1991, pp. 601–639. doi:10.1146/annurev.fl.23.010191.003125

[11] Chacin, J. M., Cantwell, B. J., and Kline, S. J., "Study of Turbulent Boundary Layer Structure Using the Invariants of the Velocity Gradient Tensor," *Experimental Thermal and Fluid Science*, Vol. 13, 1996, pp. 308–317. doi:10.1016/S0894-1777(96)00090-8

[12] Adrian, R. J., and Liu, Z.-C., "Observation of Vortex Packets in Direct Numerical Simulation of Fully Turbulent Channel Flow," *Journal of Visualization*, Vol. 5, No. 1, 2002, pp. 9–19. doi:10.1007/BF03182598

[13] Wu, X., and Moin, P., "Direct Numerical Simulation of Turbulence in a Nominally Zero- Pressure-Gradient Flat-Plate Boundary Layer," *Journal of Fluid Mechanics*, Vol. 630, 2009, pp. 5–41. doi:10.1017/S0022112009006624

[14] Schroder, A., Geisler, R., Elsinga, G. E., Scarano, F., and Dierksheide, U., "Investigation of a Turbulent Spot and a Tripped Turbulent Boundary Layer Flow Using Time-Resolved Tomographic PIV," *Experiments in Fluids*, Vol. 44, 2008, pp. 305–316. doi:10.1007/s00348-007-0403-2

[15] Sheng, J., Malkiel, E., and Katz, J., "Buffer Layer Structures Associated with Extreme Wall Stress Events in a Smooth Wall Turbulent Boundary Layer," *Journal of Fluid Mechanics*, Vol. 633, 2009, pp. 17–60. doi:10.1017/S0022112009006934

[16] Katz, J., and Sheng, J., "Applications of Holography in Fluid Mechanics and Particle Dynamics," *Annual Review of Fluid Mechanics*, Vol. 42, 2010, pp. 531–555. doi:10.1146/annurev-fluid-121108-145508

[17] Gao, Q., Ortiz-Duenas, C., and Longmire, E. K., "Eddy Structure in Turbulent Boundary Layers Based on Tomographic PIV," *15th International Symposium on Applications of Laser Techniques to Fluid Mechanics*, Lisbon, Portugal, July 2010.

[18] Elsinga, G. E., Adrian, R. J., van Oudheusden, B. W., and Scarano, F., "Three-Dimensional Vortex Organization in a High-Reynolds Number Supersonic Turbulent Boundary Layer," *Journal of Fluid Mechanics*, Vol. 644, 2010, pp. 35–60. doi:10.1017/S0022112009992047

[19] Kline, S. J., Reynolds, W. C., Schraub, F. A., and Runstadler, P. W., "The Structure of Turbulent Boundary Layers," *Journal of Fluid Mechanics*, Vol. 30, No. 4, 1967, pp. 741–773. doi:10.1017/S0022112067001740

[20] Corino, E. R., and Brodkey, R. S., "A Visual Investigation of the Wall Region in Turbulent Flow," *Journal of Fluid Mechanics*, Vol. 37, No. 1, 1969, pp. 1–30. doi:10.1017/S0022112069000395

[21] Falco, R. E., "A Coherent Structure Model of the Turbulent Boundary Layer and Its Ability to Predict Reynolds Number Dependence," *Philosophical Transactions: Physical Science and Engineering*, Vol. 336, No. 1641, 1991, pp. 103–129. doi:10.1098/rsta.1991.0069

[22] Palumbo, D., "Deriving Lifetime Maps of Coherent Structures in the Turbulent Boundary Layer," *AIAA Journal*, Vol. 46, No. 4, 2008, pp. 810–823. doi:10.2514/1.30644

[23] Adrian, R. J., "Hairpin Vortex Organization in Wall Turbulence," *Physics of Fluids*, Vol. 19, No. 4, 2007, Paper 041301. doi:10.1063/1.2717527

[24] Gao, Q., Ortiz-Duenas, C., and Longmire, E. K., "Analysis of Vortex Populations in Turbulent Wall-Bounded Flow," *Journal of Fluid Mechanics*, Vol. 678, 2011, pp. 87–123. doi:10.1017/jfm.2011.101

[25] Rist, U., and Baysal, K., "Visualization and Tracking of Vortices and Shear Layers in the Late Stages of Boundary-Layer Laminar-Turbulent Transition," AIAA Paper 2012-0084, 2012.

[26] Schafhitzel, T., Baysal, K., Rist, U., Weiskopf, D., and Ertl, T., "Particle-Based Vortex Core Line Tracking Taking into Account Vortex Dynamics," *Proceedings of ISFV13/FLUVISU 12*, Nice, France, 2008.

[27] Marusic, I., McKeon, B. J., Monkewitz, P. A., Nagib, H. M., Smits, A. J., and Sreenivasan, K. R., "Wall-Bounded Turbulent Flows at High Reynolds Numbers: Recent Advances and Key Issues," *Physics of Fluids*, Vol. 22, 2010, Paper. 065103. doi:10.1063/1.3453711

[28] Lee, C. B., and Wu, J. Z., "Transition in Wall-Bounded Flows," *Applied Mechanics Reviews*, Vol. 61, 2008, Paper 030802. doi:10.1115/1.2909605

[29] Liu, C., and Lu, P., "DNS Study on Physics of Late Boundary Layer Transition," AIAA Paper 2012-0083, 2012.

[30] Chen, L., Liu, X., Oliveira, M., and Liu, C., "DNS for Ring-Like Vortices Formation and Roles in Positive Spikes Formation," AIAA Paper 2010-1471, 2010.

[31] Lu, P., and Lin, C., "Numerical Study of Mechanism of U-Shaped Vortex Formation," AIAA Paper 2011-0286, 2011.

[32] Landahl, M. T., "A Note on an Algebraic Instability of Inviscid Parallel Shear Flows," *Journal of Fluid Mechanics*, Vol. 98, No. 2, 1980, pp. 243–251. doi:10.1017/S0022112080000122

[33] Bake, S., Meyer, D. G. W., and Rist, U., "Turbulence Mechanism in Klebanoff Transition: A Quantitative Comparison of Experiment and Direct Numerical Simulation," *Journal of Fluid Mechanics*, Vol. 459, 2002, pp. 217–243. doi:10.1017/S0022112002007954

[34] Schlatter, P., Brandt, L., de Lange, H. C., and Henningson, D. S., "On Streak Breakdown in Bypass Transition," *Physics of Fluids*, Vol. 20, 2008, Paper 101505. doi:10.1063/1.3005836

[35] Marusic, I., "Unraveling Turbulence Near Walls," *Journal of Fluid Mechanics*, Vol. 630, 2009, pp. 1–4. doi:10.1017/S0022112009007708

[36] Schoppa, W., and Hussain, F., "Coherent Structure Generation in Near-Wall Turbulence," *Journal of Fluid Mechanics*, Vol. 453, 2002, pp. 57–108. doi:10.1017/S002211200100667X

[37] Vermeersch, O., and Amal, D., "Klebanoff-Mode Modeling and Bypass-Transition Prediction," *AIAA Journal*, Vol. 48, No. 11, 2010, pp. 2491–2500. doi:10.2514/1.J050002

[38] Vaughan, N. J., and Zaki, T. A., "Stability of Zero-Pressure-Gradient Boundary Layer Distorted by Unsteady Klebanoff Streaks," *Journal of Fluid Mechanics*, Vol. 681, 2011, pp. 116–153. doi:10.1017/jfm.2011.177

[39] Tardu, F. S., Nacereddine, R., and Doche, O., "An Interactive Bypass Transition Mechanism in Wall-Bounded Flows," *Journal of Fluid Mechanics*, Vol. 615, 2008, pp. 345–369. doi:10.1017/S0022112008003728

[40] Zhou, J., Adrian, R. J., Balachandar, S., and Kendall, T. M., "Mechanisms for Generating Coherent Packets of Hairpin Vortices in Channel Flow," *Journal of Fluid Mechanics*, Vol. 387, 1999, pp. 353–396. doi:10.1017/S002211209900467X

[41] Stanislas, M., Perret, L., and Foucaut, J.-M., "Vortical Structures in the Turbulent Boundary Layer: A Possible Route to a Universal Representation," *Journal of Fluid Mechanics*, Vol. 602, 2008, pp. 327–382. doi:10.1017/S0022112008000803

[42] Natrajan, V. K., Wu, Y., and Christensen, K. T., "Spatial Signatures of Retrograde Spanwise Vortices in Wall Turbulence," *Journal of Fluid Mechanics*, Vol. 574, 2007, pp. 155–167. doi:10.1017/S0022112006003788

[43] Dennis, D. J. C., and Nickels, T. B., "Experimental Measurement of Large-Scale Three-Dimensional Structures in a Turbulent Boundary Layer. Part 1. Vortex Packets," *Journal of Fluid Mechanics*, Vol. 673, 2011, pp. 180–217. doi:10.1017/S0022112010006324

[44] Martin, J. E., and Meiburg, E., "Numerical Investigation of Three-Dimensionally Evolving Jets Subject to Axisymmetric and Azimuthal Perturbations," *Journal of Fluid Mechanics*, Vol. 230, 1991, pp. 271–318. doi:10.1017/S0022112091000794

[45] Bernard, P. S., "Vortex Filament Simulation of the Turbulent Coflowing Jet," *Physics of Fluids*, Vol. 21, 2009, Paper 025107. doi:10.1063/1.3081559

[46] Ashurst, W. T., and Meiburg, E., "Three-Dimensional Shear Layers via Vortex Dynamics," *Journal of Fluid Mechanics*, Vol. 189, 1988, pp. 87–116. doi:10.1017/S0022112088000928

[47] Bernard, P. S., "Grid-Free Simulation of the Spatially Growing Mixing Layer," *AIAA Journal*, Vol. 46, No. 7, 2008, pp. 1725–1737. doi:10.2514/1.34205

[48] Bernard, P. S., Collins, P., and Potts, M., "Vortex Filament Simulation of the Turbulent Boundary Layer," *AIAA Journal*, Vol. 48, No. 8, 2010, pp. 1757–1771. doi:10.2514/1.J050224

[49] Bernard, P. S., "The Hairpin Vortex Illusion," *Journal of Physics: Conference Series*, Vol. 318, 2011, Paper 060024. doi:10.1088/1742-6596/318/6/062004

[50] Bernard, P. S., "Turbulent Flow Properties of Large Scale Vortex Systems," *Proceedings of the National Academy of Sciences of the United States of America*, Vol. 103, No. 27, 2006, pp. 10174–10179. doi:10.1073/pnas.0604159103

[51] Chorin, A. J., "Hairpin Removal in Vortex Interactions II," *Journal of Computational Physics*, Vol. 107, 1993, pp. 1–9. doi:10.1006/jcph.1993.1120

[52] Chorin, A. J., *Vorticity and Turbulence*, Springer–Verlag, New York, 1994, pp. 144–155.

[53] Greengard, L., and Rokhlin, V., "A Fast Algorithm for Particle Simulations," *Journal of Computational Physics*, Vol. 73, No. 2, 1987, pp. 325–348. doi:10.1016/0021-9991(87)90140-9

[54] Strickland, J. H., and Baty, R. S., "A Three-Dimensional Fast Solver for Arbitrary Vorton Distributions," Sandia National Lab. Rept SAND93-1641, 1994.

[55] Spyropoulos, E. T., and Blaisdell, G. A., "Large-Eddy Simulation of a Spatially Evolving Supersonic Turbulent Boundary-Layer Flow," *AIAA Journal*, Vol. 36, No. 11, 1998, pp. 1983–1990. doi:10.2514/2.325

[56] Sreenivasan, K. R., "On the Universality of the Kolmogorov Constant," *Physics of Fluids*, Vol. 7, No. 11, 1995, pp. 2778–2784. doi:10.1063/1.868656

[57] Spalart, P. R., "Direct Simulation of a Turbulent Boundary Layer up to $R_\theta = 1410$," *Journal of Fluid Mechanics*, Vol. 187, 1988, pp. 61–98. doi:10.1017/S0022112088000345

[58] Acarlar, M. S., and Smith, C. R., "A Study of Hairpin Vortices in a Laminar Boundary Layer. Part 1. Hairpin Vortices Generated by a Hemisphere Protuberance," *Journal of Fluid Mechanics*, Vol. 175, 1987, pp. 1–41. doi:10.1017/S0022112087000272

[59] Seal, C. V., and Smith, C. R., "Visualization of a Mechanism for Three-Dimensional Interaction and Near-Wall Eruption," *Journal of Fluid Mechanics*, Vol. 394, 1999, pp. 193–203. doi:10.1017/S0022112099005571

[60] Smits, A. J., McKeon, B. J., and Marusic, I., "High-Reynolds Number Wall Turbulence," *Annual Review of Fluid Mechanics*, Vol. 43, 2011, pp. 353–375. doi:10.1146/annurev-fluid-122109-160753

[61] Kim, K., Sung, H. J., and Adrian, R. J., "Effects of Background Noise on Generating Coherent Packets of Hairpin Vortices," *Physics of Fluids*, Vol. 20, 2008, Paper 105107. doi:10.1063/1.3001797

[62] Panton, R. L., "Overview of the Self-Sustaining Mechanisms of Wall Turbulence," *Progress in Aeronautical Science*, Vol. 37, No. 4, 2001, pp. 341–383. doi:10.1016/S0376-0421(01)00009-4

[63] Kim, J., Moin, P., and Moser, R., "Turbulence Statistics in Fully Developed Channel Flow at Low Reynolds Number," *Journal of Fluid Mechanics*, Vol. 177, 1987, pp. 133–166. doi:10.1017/S0022112087000892

[64] Rist, U., and Fasel, H., "Direct Numerical Simulation of Controlled Transition in a Flat-Plate Boundary Layer," *Journal of Fluid Mechanics*, Vol. 298, 1995, pp. 211–248. doi:10.1017/S0022112095003284

X. Zhong
Associate Editor